COMPUTATION OF LAMINAR VISCOUS-INVISCID INTERACTIONS IN HIGH-SPEED INTERNAL FLOWS

David H. Rudy
James L. Thomas
Ajay Kumar
NASA Langley Research Center
Hampton, VA 23665

ABSTRACT

A review is given of computations for a series of nominally two-dimensional laminar viscous-inviscid interactions. Comparisons were made with detailed experimental shock-tunnel results. The shock wave-boundary layer interactions considered were induced by a compression ramp in one case and by an externally-generated incident shock in the second case. In general, good agreement was reached between the grid-refined calculations and experiment for the incipient- and small-separation conditions. For the highly separated flow, three-dimensional calculations which included the finite-span effects of the experiment were required in order to obtain agreement with the data.

NOMENCLATURE

C_f	skin-friction coefficient, $2\tau_w/\rho_\infty u_\infty^2$
C_h	heat-transfer coefficient, $\dot{q}/\rho_\infty u_\infty (H_\infty - H_w)$
C_p	pressure coefficient, $2p/\rho_\infty u_\infty^2$
H	total enthalpy
L	reference length
M	Mach number
p	pressure
$\dot{q}$	heat-transfer rate
Re	unit Reynolds number, $\rho_\infty u_\infty/\mu_\infty$
T	temperature
u	streamwise velocity
x	streamwise coordinate
β	shock angle
γ	ratio of specific heats
θ	compression-ramp or wedge angle
μ	molecular viscosity
ρ	density
τ	shear stress

subscripts

att	reattachment point
sep	separation point
w	wall
∞	free stream

INTRODUCTION

The propulsion system of advanced hypersonic vehicles will likely use the external vehicle contours as compression and expansion surfaces for the inlet and nozzle, respectively. Thus, the integration of the engine and airframe is an important design consideration. This design process relies heavily upon the development of computer codes with appropriate geometric flexibility and physical models since many of the high Mach-number, high enthalpy flow conditions the vehicle may encounter in flight cannot presently be simulated in ground-based facilities. Part of the process of validating such a code is to assess the code's ability to simulate the complex physics of the vehicle flow field by making

comparisons of computed results with available benchmark experimental data. The present paper summarises the results of such comparisons for two types of shock-boundary layer interactions that can occur in the forebody and inlet portions of the vehicle.

DESCRIPTION OF CODES

The main code used in these studies was CFL3D (Computational Fluids Laboratory 3-D code), which was developed by J. L. Thomas for the thin-layer Navier-Stokes equations and is described in reference 1. This code uses a finite-volume method in which the convective and pressure terms are discretised with the upwind-biased flux-difference splitting technique of Roe. The reconstruction of the cell-centered variables to the cell-interface locations is done using a monotone interpolation of the primitive variables such that third-order accuracy in one-dimensional inviscid flow is obtained. The differencing for the diffusion terms representing shear stress and heat transfer effects corresponds to second-order-accurate central differencing so that the global spatial accuracy of the method is second order. The time-differencing algorithm is a spatially-split approximate-factorisation scheme.

Three other codes were used for comparison with the CFL3D results. Two of these codes use similar recently-developed upwind technology. One was USA-PG2 (Unified Solution Algorithm-Perfect Gas, 2-D), which was developed by S. R. Chakravarthy and is described in reference 2. The other was LAURA (Langley Aerothermodynamic Upwind Relaxation Algorithm), which was developed by P. A. Gnoffo and is described in reference 3. The fourth code, NASCRIN (Numerical Analysis of SCRamjet INlets), was developed by Kumar (refs. 4 and 5) and uses the original unsplit explicit finite-difference technique of MacCormack (ref. 6) to solve the full Navier-Stokes equations. This technique is a two-step, predictor-corrector scheme which is second-order accurate in both space and time. Fourth-order artificial viscosity based on the gradients of pressure and temperature is used near shock waves to suppress numerical oscillations. This code has been previously used to compute a variety of inlet flow fields.

TEST CASES

The two test cases considered in the present study are shown schematically in Fig. 1. Both of these cases are hypersonic flows with viscous/inviscid interactions typical of those found in the flow field within the propulsion system of a hypersonic vehicle. The first of these test cases was the two-dimensional flow over a compression corner formed by the intersection of a flat plate and a wedge tested by Holden and Moselle (ref. 7) in the Calspan 48-inch Shock Tunnel. The flow field shown in Fig. 1(a) shows the separated flow which forms in the corner region for a sufficiently large wedge angle. Downstream of the reattachment point, the boundary layer thins rapidly due to the compression, resulting in large increases in skin friction and heat transfer on the wedge surface. Furthermore, the compression waves produced by the corner coalesce into a shock wave which intersects with the leading-edge shock, producing an expansion fan and a shear layer, both of which affect the flow on the ramp. Three wedge angles tested by Holden and Moselle are considered here. The flow remained attached on the 15-degree wedge, a small separated-flow region occurred with the 18-degree wedge, and a large separated-flow region was produced by the 24-degree wedge.

The nominal flow conditions for this case were $M_\infty = 14.1$, $T_\infty = 160^o R$, and $Re = 7.2\text{x}10^4$ per foot. The wall temperature, T_w, was $535^o R$. The Reynolds number was low enough that the flow remained completely laminar, thereby eliminating the issue of turbulence modeling from the present study. Furthermore, even though the free-stream Mach number was high, the free-stream temperature was low enough that there were no significant real-gas effects. In the experiment, values of surface pressure, skin friction, and heat transfer were measured in the centerplane of the model which had a spanwise length that was thought to be sufficient to produce two-dimensional flow in the measurement region.

The second test case, shown in Fig. 1(b), was the interaction of an incident shock produced by a shock-generator wedge with a flat-plate boundary layer in hypersonic flow. The features of this flow field are very similar to those produced by the compression corner. In this case, the incident shock produces a separated-flow region. Downstream of this region, the boundary layer thins rapidly due to the compression. As in the first case, measurements were made in the centerplane of the model which had a spanwise length judged sufficient to produce two-dimensional flow in the measurement region. The experimental data were obtained by Holden (ref. 8) in the Calspan 48-inch Shock Tunnel. The nominal flow conditions for this case were $M_\infty = 15.6$, $T_\infty = 77^o R$, and $Re = 1.36\text{x}10^5$ per foot. The wall temperature, T_w, was $535^o R$. Solutions were computed for two different shock-generator wedge angles, 4.017^o and 6.45^o. As in the compression-corner experiments, the flow was completely laminar and real gas effects were not significant.

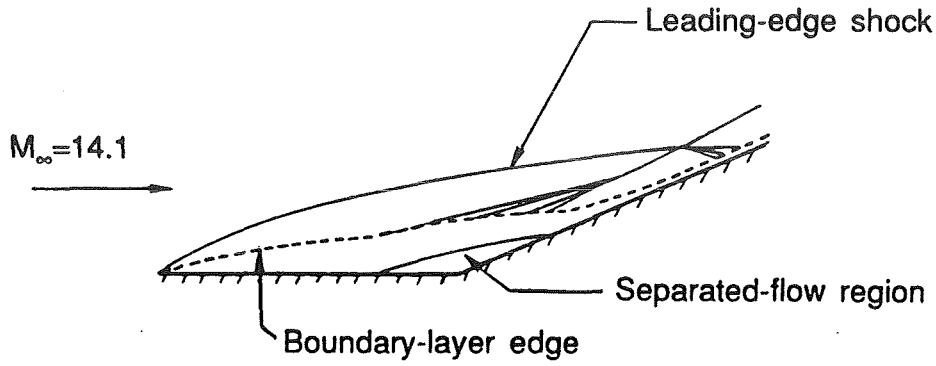

(a.) Compression corner.

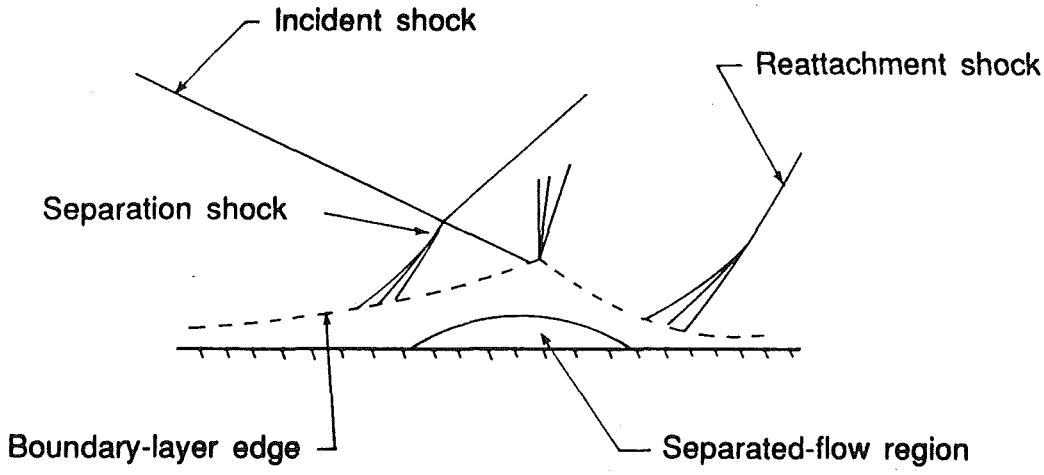

(b.) Shock-boundary layer interaction.

Fig. 1 Test cases.

RESULTS AND DISCUSSION

Compression-corner case

Comparisons were made between the computed solutions from all four codes and experimental data for the 15- and 24-degree wedges using two different grids. (The flow over the 18-degree wedge was computed only with CFL3D, and this result will be shown in the summary plots.) The first grid had 51 points in the streamwise direction and 51 points in the vertical direction. The upper boundary of the grid was parallel to the lower boundary. In the streamwise direction, the grid was clustered near the leading edge of the flat plate and in the corner region. In the normal direction, the grid was clustered near the model surface. Above the wedge, a simple sheared grid was used, producing a non-orthogonal grid in this region. A second grid with twice the resolution was constructed from the first grid using 101 points in each direction while maintaining the same grid stretching. The 101 x 101 grid for the 24-degree wedge is shown in Fig. 2. Calculations were made for other grids using only CFL3D. Additional details for the compression-corner study beyond those summarized below are given in reference 9.

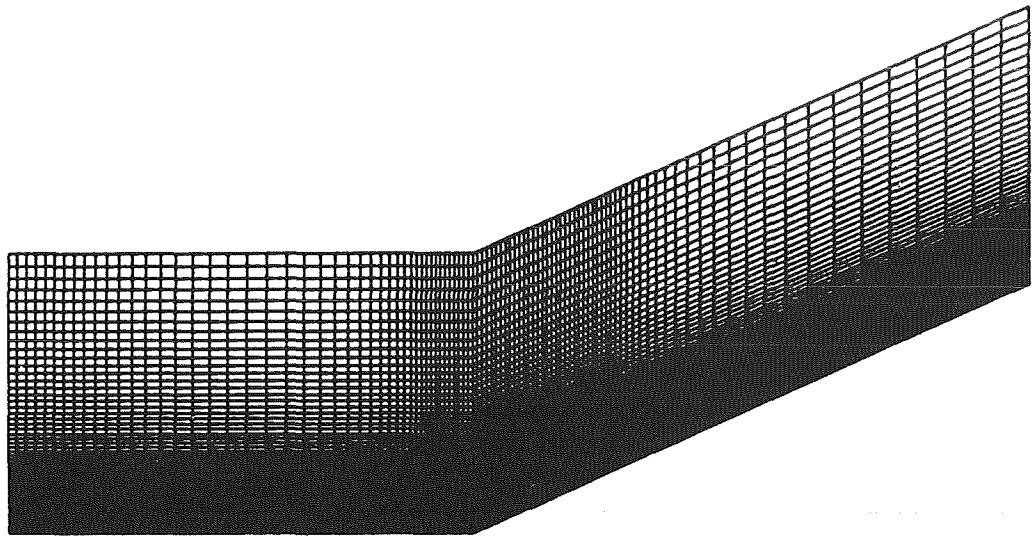

Fig. 2 Grid for 24-degree wedge. 101 x 101.

15° wedge. Fig. 3(a) shows a comparison of the computed surface-pressure coefficient with experimental values for all four codes on two different grids. The pressure coefficient is plotted as a function of x/L, where x is measured from the leading edge of the flat plate and L is the length of the flat-plate portion of the model. It should be noted that all of the plots shown in the present paper for the compression-corner case differ from those given in reference 9 in two ways. First of all, the experimental data have been revised by Holden, who recomputed the free-stream conditions using the tunnel calibration rather than using pitot-tube measurements from the experiment. The resulting change in the surface coefficient data eliminated the need for the one-degree angle-of-attack correction which was necessary in reference 9 to match the experimental values of pressure on the flat-plate portion of the model. Secondly, the data were originally given in reference 7 as a function of the distance along the surface of the model but were interpreted as being a function of the streamwise distance x in the plots in reference 9. Thus, the data on the ramp in reference 9 were shifted slightly downstream from their correct location. As shown in Fig. 3(a), there are only very slight differences in the predictions from the codes for the 51 x 51 grid; however, the solutions are virtually identical for the 101 x 101 grid. The computed pressures are generally higher than the experimental values even on the flat-plate portion of the model. However, the computed pressures were in excellent agreement with those given by hypersonic strong-interaction theory (not shown). The corresponding comparison of the computed surface heat-transfer coefficient with experimental values for all four codes on the two grids is shown in Fig. 3(b). As with the pressure coefficient, the calculations on the 101 x 101 grid produce the best agreement among the codes. The largest differences occur along the ramp.

24° wedge. Fig. 4 shows the comparison of the computed surface-pressure coefficient with experimental values for this case. The codes predict different extents of separation even with the 101 x 101 grid. A solution using a 201 x 201 grid was also made with CFL3D. The predictions for surface pressure, skin friction, and surface heat transfer for this grid were almost identical to those found with the 101 x 101 grid with only a slight increase in the predicted extent of separation. All of the codes demonstrated a trend with grid convergence towards a similar longitudinal extent of separation which is much larger than that found in the experiment. As a result of the larger separation extent, the shock interaction is altered, moving the peak value of pressure on the ramp downstream in comparison to the experiment.

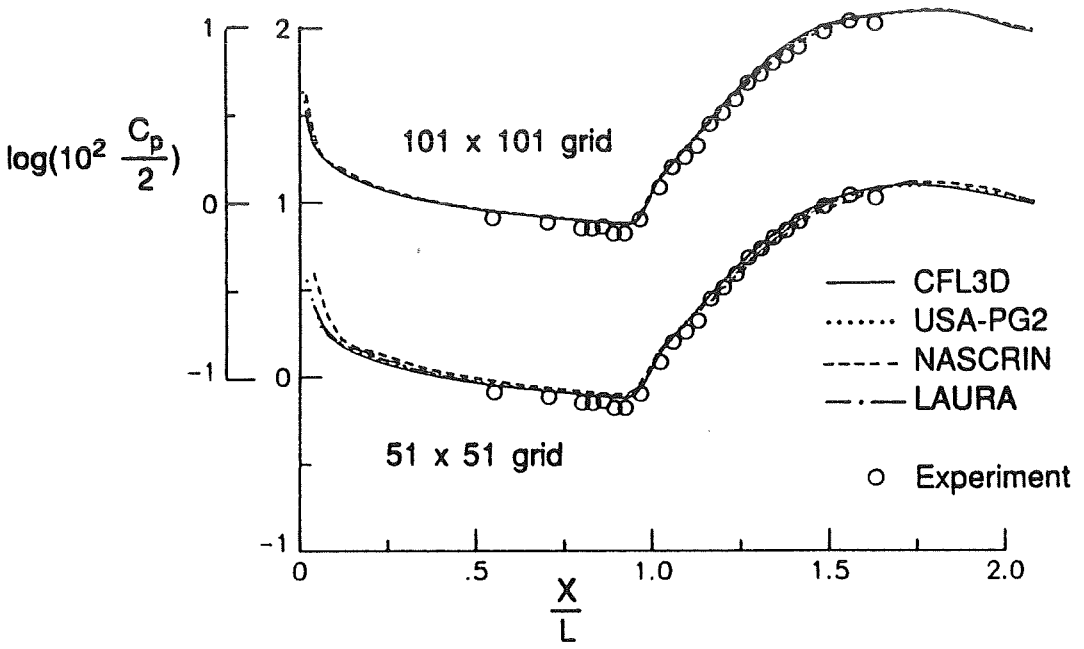

(a.) Surface pressure

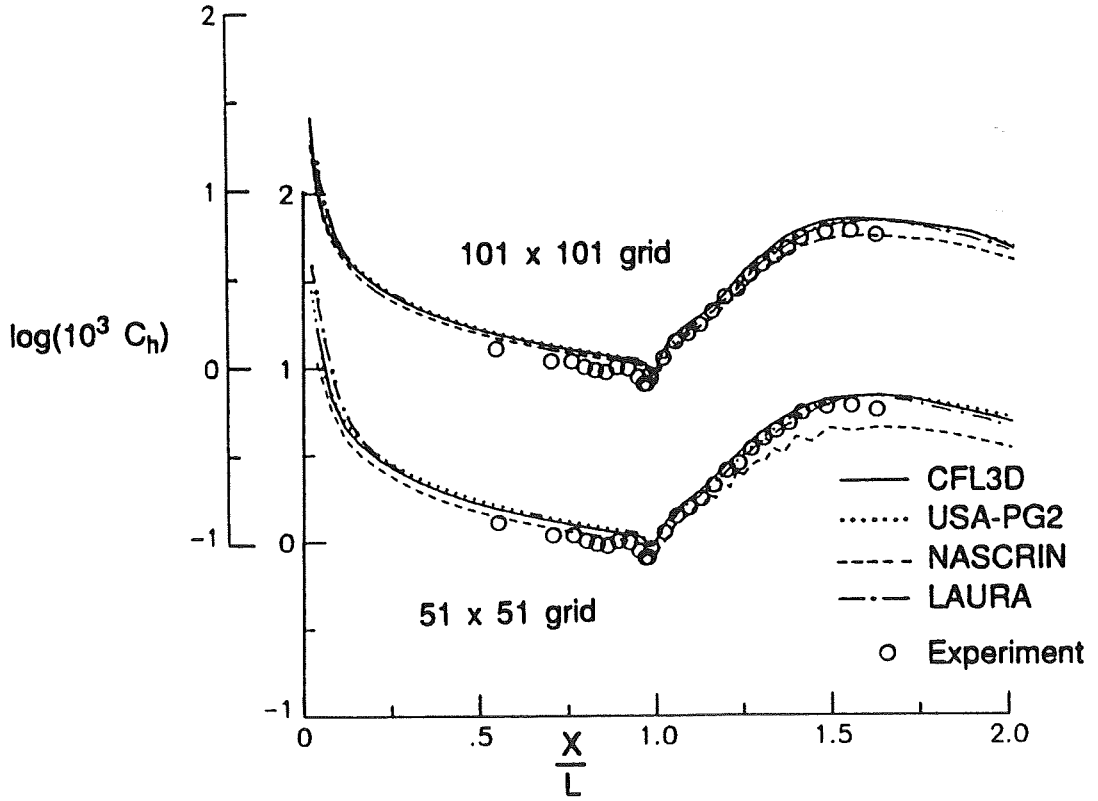

(b.) Surface heat transfer

Fig. 3 Comparison of computation and experiment for 15° wedge.

Since the results from the two-dimensional computations did not match the experimental data, 3-D calculations were made with CFL3D to investigate the possibility of flow in the spanwise direction affecting the flow in the center of the plate. For the experimental data for which comparisons are shown, no side plates were used. The spanwise length of the plate was 2 ft. Calculations were made with two different grids, 51 x 51 x 25 and 101 x 101 x 25. Because the flow is symmetric about the centerplane, the computational domain included only half of the plate. The spanwise grid contained 19 points on the plate and 6 points in the free stream. Approximate supersonic outflow boundary conditions were used at the sides of the computational domain outside of the ramp surface. Fig. 5 shows results from the calculation with a 101 x 101 grid in each streamwise plane. The streamlines in the flow very near the model surface are visualized using particle traces. The separation and reattachment lines show that the size of the separated-flow region decreases across the plate from the centerplane to the edge. The pressure contours in the downstream plane on the ramp at the end of the computational domain show an expansion of the flow in the spanwise direction near the edge of the plate to reduce the pressure to the free-stream value. A comparison of the computed 2-D and 3-D centerplane surface-pressure distributions with experimental data are shown in Fig. 6 using solutions from CFL3D. As shown, the three-dimensional effects produce a smaller separated-flow region in the centerplane than that predicted in the 2-D calculations. The size of the separated-flow region and the pressure level in that region are in excellent agreement with the data for the finest mesh in the 3-D calculation. Furthermore, in the 3-D computation, the time to establish steady-state conditions was approximately 4 ms, which is in agreement with the experiment. However, it took more than 12 ms to establish steady flow in the 2-D computations (ref. 9). The importance of the flow in the spanwise direction on the size of the separation region was shown experimentally by Putnam (ref. 10) for laminar flow over a series of compression ramps with varying span lengths at Mach 10.03. He found that decreasing the span of the ramp produced an almost linear decrease in the size of the separation region for any given ramp deflection angle.

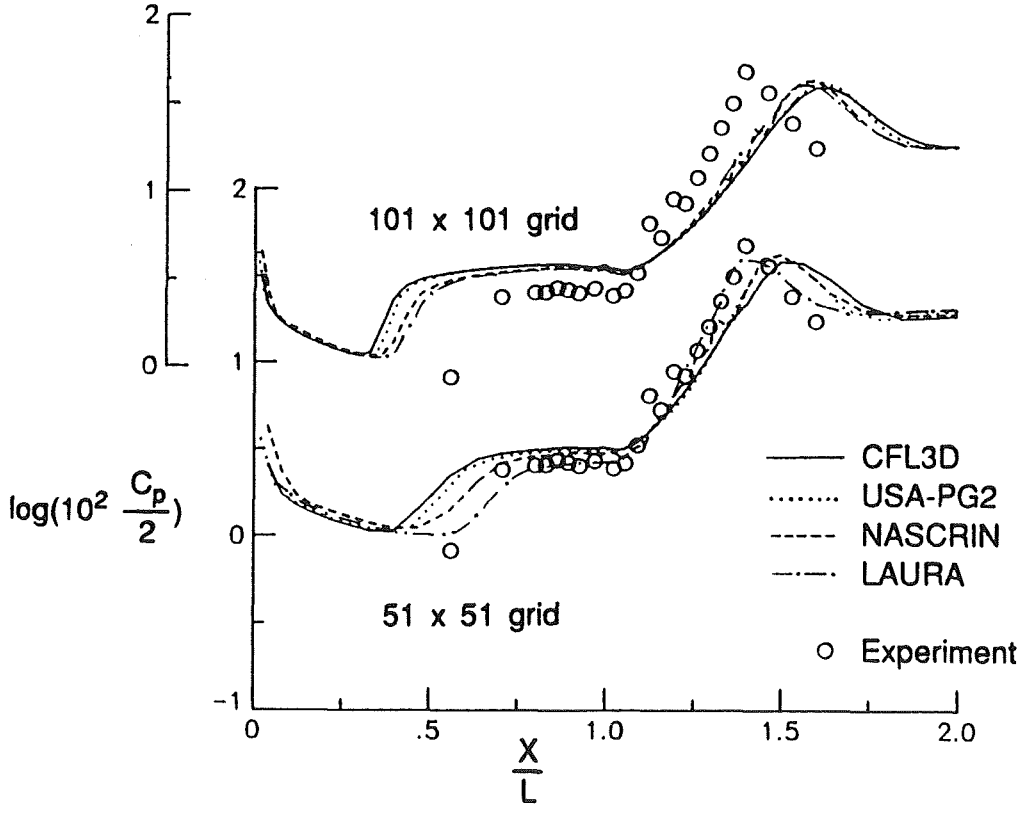

Fig. 4 Comparison of computed and experimental surface pressure for 24° wedge.

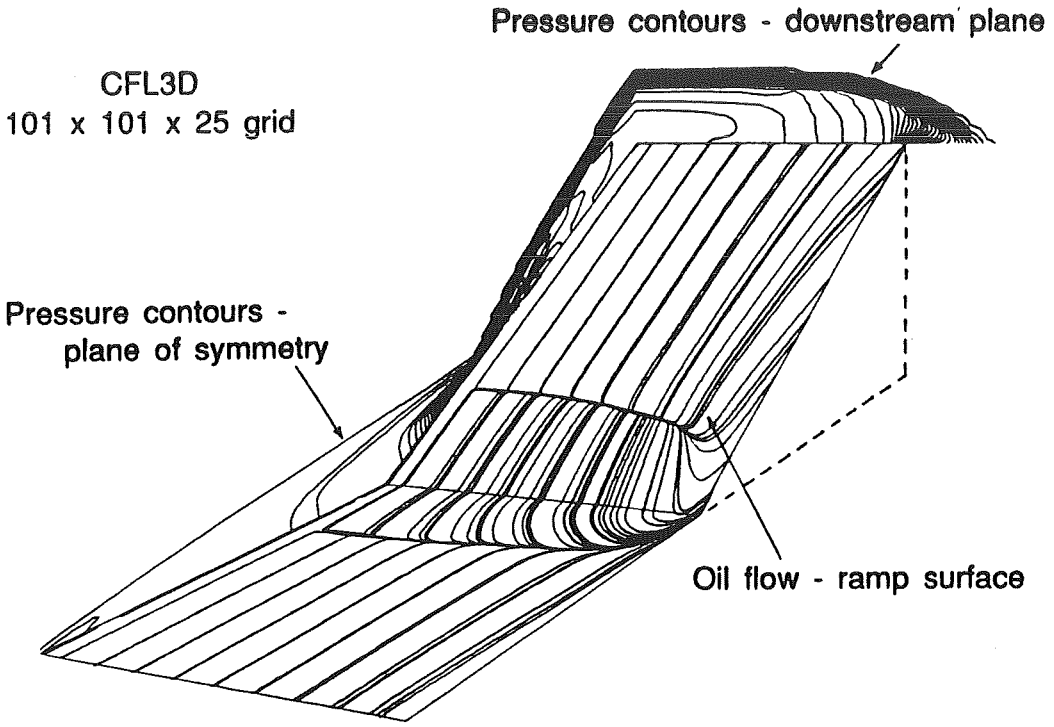

Fig. 5 3-D solution using CFL3D for 24° wedge.

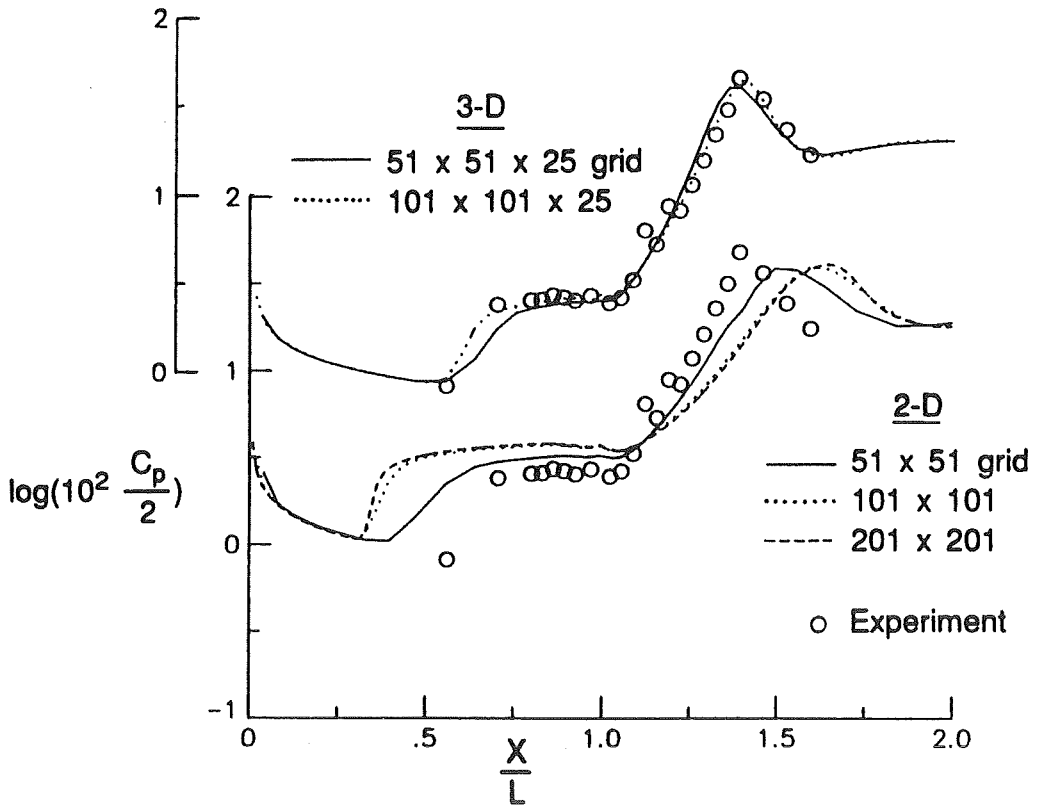

Fig. 6 Comparison of CFL3D computations and experiment for surface pressure for 24° wedge.

Two-dimensional calculations were also made for the 24-degree wedge with CFL3D using the grid topology shown in Fig. 7 which was used by Thareja et al. (ref. 11) in their study of this same test case. In this grid, the spacing in the streamwise direction remained the same as in the previous grid; however, the upper boundary in the normal direction was moved closer to the model surface and the boundary above the flat-plate portion was approximately parallel to the leading edge shock. The cell heights were reduced by a factor of approximately 17 at the leading edge and by a factor of 2.5 at the outflow boundary from those heights in the original grid. Thareja et al. (ref. 11) found that using this grid topology with 101 points in each direction, CFL3D predicted a separated-flow region closer in size to that found experimentally than with the original 101 x 101 grid. Those calculations were repeated in the present study for this 101 x 101 grid as well as for the corresponding 51 x 51 and 201 x 201 grids. The separation extent predicted in these cases is compared in Fig. 8 to the corresponding predictions for the original grids. For each grid topology, a grid density can be found which will produce a separation region that matches the experiment. Surprisingly, the results also indicate that the computations with the wedge outer boundary are less accurate for a given number of points than the computations with the rectangular outer boundary, even though the former has uniformly smaller spacing in the normal direction. Since the axial spacing is the same for both meshes, the resulting cell aspect ratio is substantially higher on the grid with the wedge outer boundary, which may be adversely affecting the spatial convergence. However, for both grid topologies, uniform refinement of the grid spacing increases the size of the separated-flow region. As the number of points is increased, the solutions produced by the two grid topologies appear to be approaching the same limit.

Thareja et al. (ref. 11) also made 2-D computations for the 24-degree wedge with their own upwind scheme using an unstructured adapted mesh developed from the second grid topology. The mesh had quadrilateral elements near the model surface and triangular elements elsewhere. The error indicator for the adaptive remeshing used a combination of second derivatives of density, velocity, and Mach number. Their two-dimensional calculations gave results in excellent agreement with the experimental data, leading Thareja et al. to question the conclusions of reference 9 that the flow was actually three-dimensional in this case. Studies are continuing to better understand why the structured and adaptive unstructured grids give different solutions.

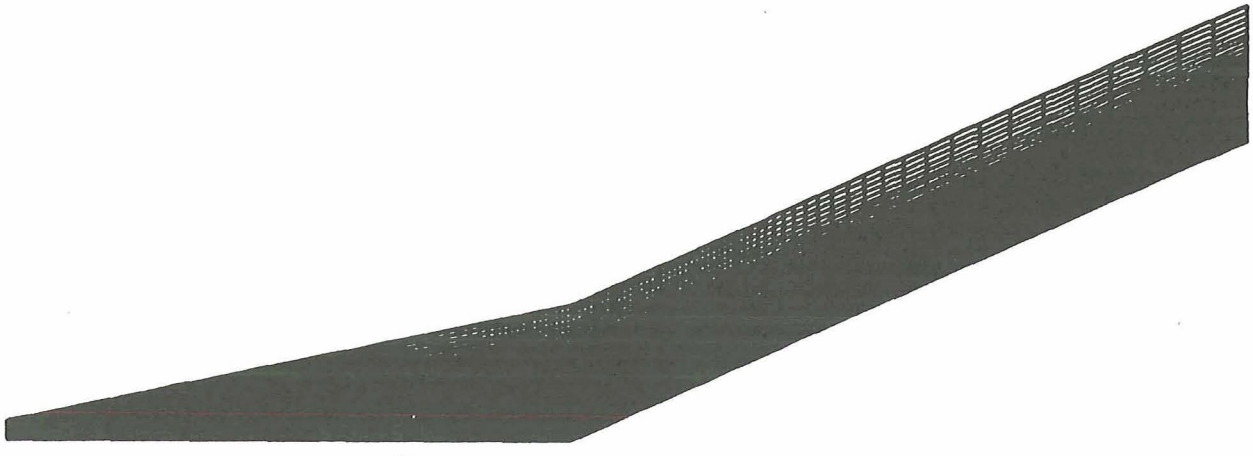

Fig. 7 Grid with wedge outer boundary. 101 x 101.

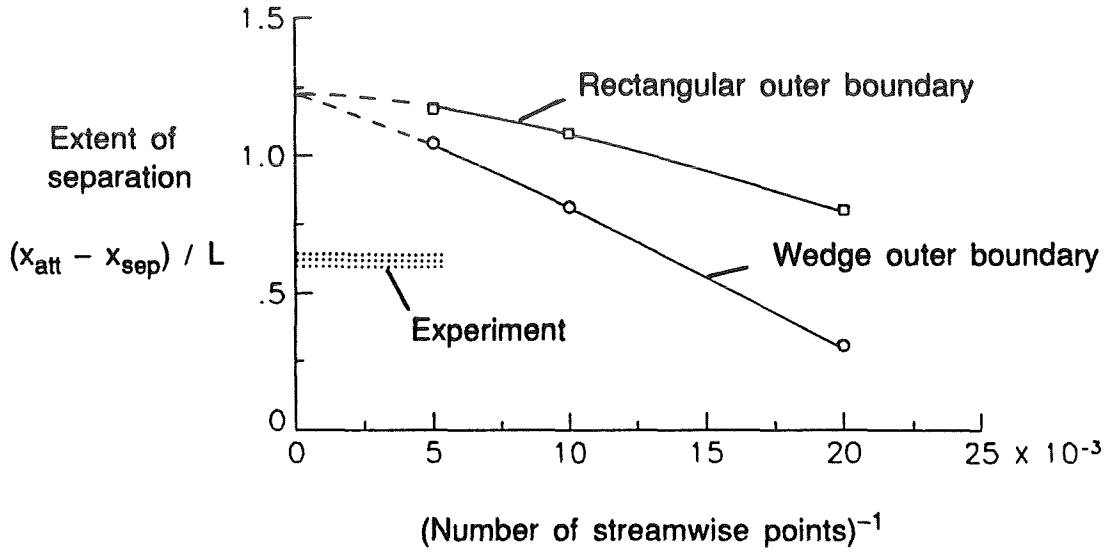

Fig. 8 Effect of grid topology and spacing on extent of separation predicted by CFL3D for 24° wedge.

Summary comparisons. Fig. 9 shows a summary comparison of the CFL3D solutions with experimental data for all three wedges. The 3-D solution in the centerplane is shown for the 24-degree wedge, and 2-D solutions are shown for both the 15- and 18-degree cases. Use of the revised experimental data in these plots eliminated the need for the angle-of-attack correction which was applied in reference 9. Excellent agreement of the calculations with experimental data was found for pressure, heat transfer, and skin friction for all three wedge angles.

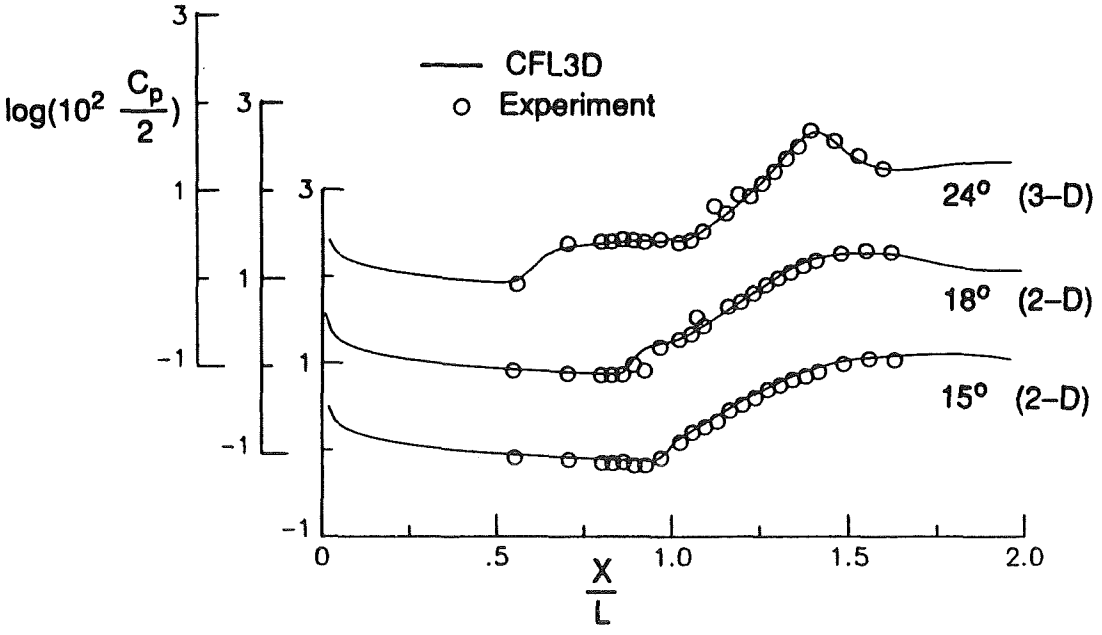

(a.) Surface pressure

Fig. 9 Summary comparison of CFL3D computations with experimental data.

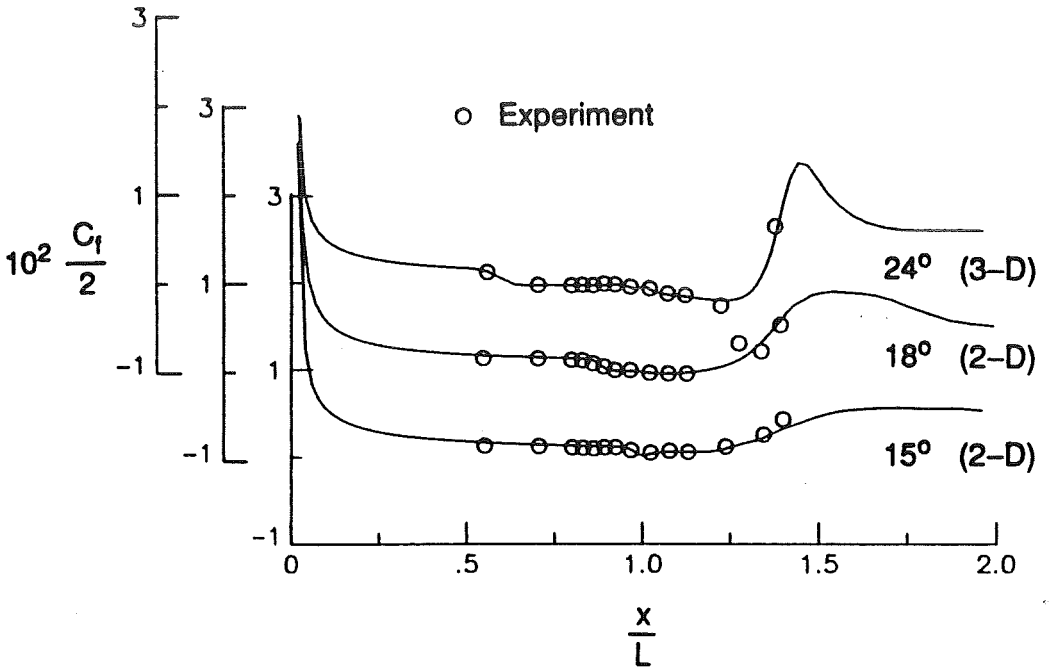

(b.) Skin friction

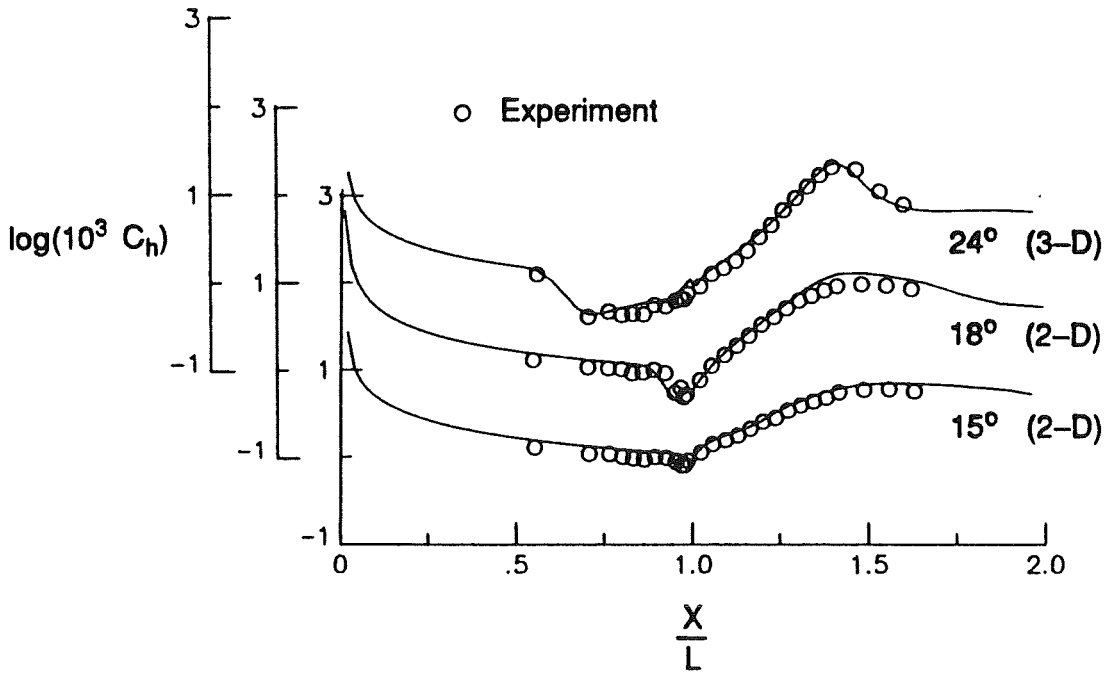

(c.) Surface heat transfer

Fig. 9 Concluded.

Shock-boundary layer interaction case

Computations were made for two of the five shock-generator-wedge angles tested by Holden at $M_\infty = 15.6$. These angles were 4.017° and 6.45°, which represent the smallest and the next-to-the-largest angles tested. The first set of calculations was made in two parts. The flow over the shock-generator wedge was computed separately using CFL3D. The shock angle obtained from this calculation was then used to specify the flow at the upper boundary of the computational domain used to compute flow over the flat plate. For $\theta = 4.017°$, computations were made using three of the codes. For $\theta = 6.45°$, computations were made using only CFL3D and USA-PG2. The grid for the flat plate had 151 points in the streamwise direction which were clustered near the leading edge of the plate and in the shock-boundary layer interaction region. The grid in the normal direction extended 3 inches above the surface of the plate and had 81 points which were clustered near the wall. For $\theta = 4.017°$, the shock angle, β, was 8°, and the shock crossed the upper boundary at the grid point at x=0.912 inches. In this case, the shock position required to properly match the experimentally-observed shock-impingement location was actually upstream of that estimated from the analysis of the computed shock-generator-wedge flow field. For $\theta = 6.45°$, the shock angle was 10.5° and the shock crossed the upper boundary at the grid point at x=6.429 inches.

A comparison of the computed surface-pressure coefficient with experimental data for both wedge angles is shown in Fig. 10. The results for the two upwind codes are virtually identical. The pressure rise in the interaction region computed by NASCRIN occurs slightly downstream of the upwind predictions. This difference is a consequence of the shock wave being introduced along the upper boundary one-half grid cell further downstream in the finite-difference method than in the upwind methods. The expansion downstream of the interaction region is not predicted for either wedge angle by any of the methods.

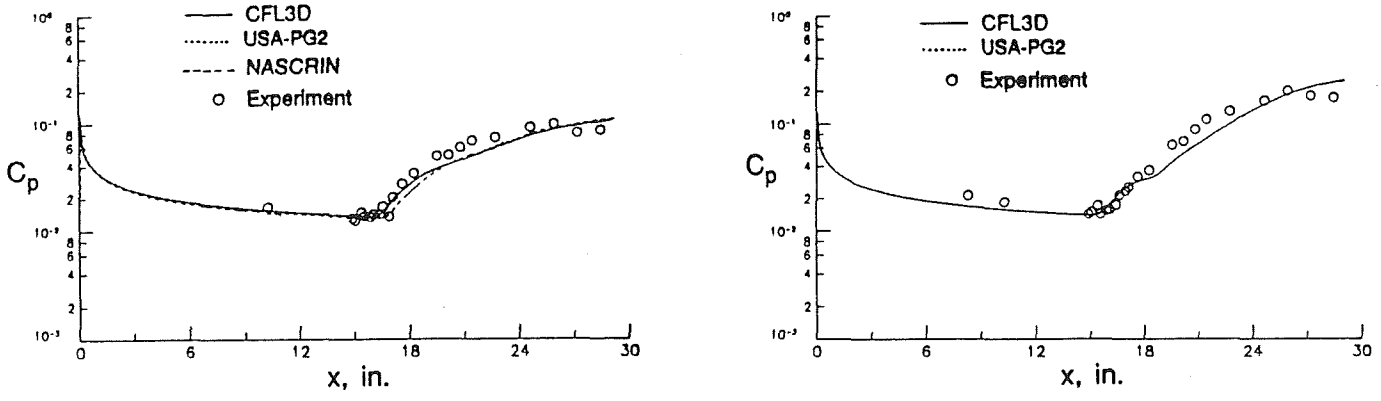

(a.) $\theta = 4.017°$

(b.) $\theta = 6.45°$

Fig. 10 Comparison of computed and experimental surface pressure for shock-boundary layer interaction.

Computations were also made using CFL3D which included the flow over the shock generator wedge as well as the flow over the plate as part of a single simulation. The grid for this case is shown in Fig. 11(a). The grid over the flat plate remained the same as in the previous calculations, and the grid near the wedge contained the same amount of clustering in the normal direction as the grid near the plate. The grid contained 191 points in the streamwise direction and 151 points in the normal direction. The upper boundary downstream of the trailing edge of the shock generator wedge was simulated as a flat plate parallel to the free-stream flow. Contours of pressure and Mach number for the $\theta = 6.45^o$ simulation are shown in Figs. 11(b) and (c), respectively. The pressure contours illustrate the intersection of the wedge and flat-plate leading-edge shocks as well as the interaction of the wedge shock with the flat-plate boundary layer. The Mach-number contours highlight the boundary-layer development and the shock waves and also indicate a separation zone in the interaction region on the lower flat plate. The corresponding calculation for the case with $\theta = 4.017^o$ produced a wedge shock which impinged on the flat-plate boundary layer downstream of the measured impingement, consistent with the observation noted above for the specified-shock calculations. To match the experimentally-observed impingement location, the height of the trailing edge of the shock-generator wedge above the flat plate was changed from the value of 3.625 inches reported for the experimental configuration to 3.242 inches.

Fig. 12 shows a comparison of the surface-pressure coefficient for the specified-shock calculation and the complete flow-field simulation using CFL3D for $\theta = 6.45^o$. The only difference between the two results occurs downstream of the interaction where the complete simulation captures the expansion produced by the flow from the trailing edge of the generator wedge.

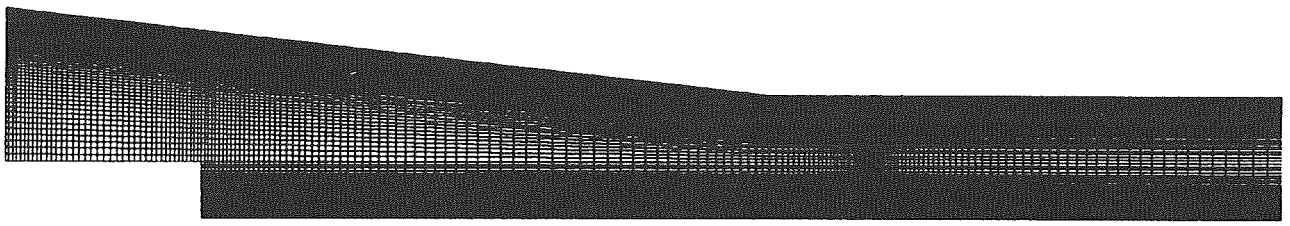

(a.) Grid

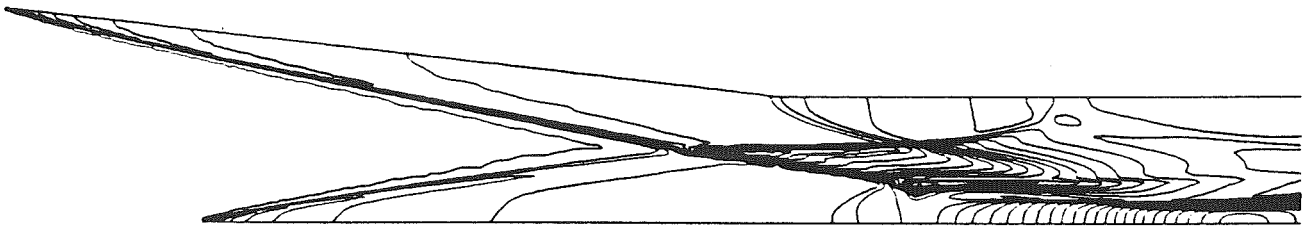

(b.) Pressure

Fig. 11 Grid and computed flow field for CFL3D simulation of complete configuration. $\theta = 6.45^o$.

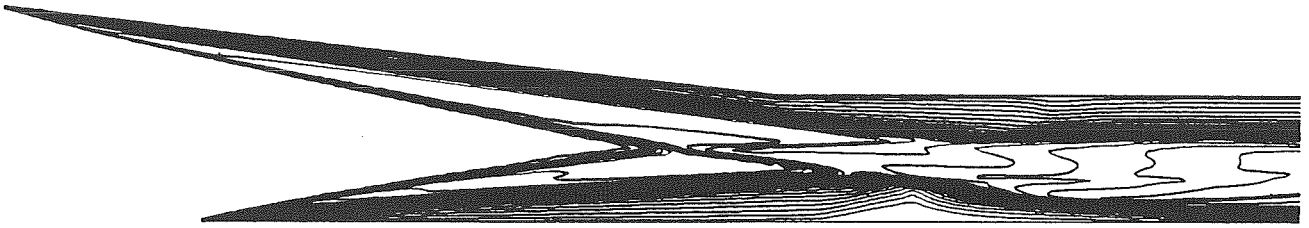

(c.) Mach number

Fig. 11 Concluded

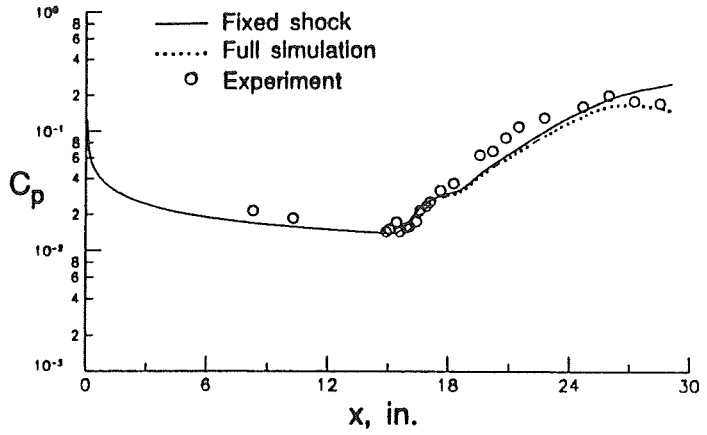

Fig. 12 Comparison of fixed-shock and complete flow-field CFL3D computations. $\theta = 6.45°$.

CONCLUDING REMARKS

Computations for a series of nominally two-dimensional high-speed laminar separated flows were compared with detailed experimental shock-tunnel results. The shock wave-boundary layer interactions considered were induced by a compression ramp in one case and by an externally-generated incident shock in the second case. In general, good agreement was reached between the grid-refined calculations and experiment for the incipient- and small-separation conditions. For the most highly separated flow, three-dimensional calculations which included the finite-span effects of the experiment were required in order to obtain agreement with the data. The finite-span effects were important in determining the extent of separation as well as the time required to establish the steady-flow interaction.

REFERENCES

1. Vatsa, V. N., Thomas, J. L. and Wedan, B. W., "Navier-Stokes Computations of Prolate Spheroids at Angle of Attack," AIAA Paper 87-2627CP (1987).

2. Chakrarthy, S. R., Ssema, K.-Y., Goldberg, U., Gorski, J. J. and Osher, S., "Application of a New Class of High Accuracy TVD Schemes to the Navier-Stokes Equations," AIAA Paper 85-0165 (1985).

3. Gnoffo, Peter. A., "Upwind-Biased, Point-Implicit Relaxation Strategies for Viscous Hypersonic Flow," AIAA Paper 89-1972CP (1989).

4. Kumar, A., "Numerical Simulation of Scramjet Inlet Flow Fields," NASA TP-2517 (1986).

5. Kumar, A., "User's Guide for NASCRIN - A Vectorised Code for Calculating Two-Dimensional Supersonic Internal Flow Fields," NASA TM-85708 (1984).

6. MacCormack, R. W., "The Effect of Viscosity in Hypervelocity Impact Cratering," AIAA Paper 69-354 (1969).

7. Holden, M. S. and Moselle, J. R., "Theoretical and Experimental Studies of the Shock Wave-Boundary Layer Interaction on Compression Surfaces in Hypersonic Flow," ARL 70-0002 (1970).

8. Holden, M. S., "A Study of Flow Separation in Regions of Shock Wave-Boundary Layer Interaction in Hypersonic Flow," AIAA Paper 78-1169 (1978).

9. Rudy, D. H., Thomas, J. L., Kumar, A., Gnoffo, P. A. and Chakravarthy, S. R., "A Validation Study of Four Navier-Stokes Codes for High-Speed Flows," AIAA Paper 89-1838 (1989).

10. Putnam, L. E., "Investigation of Effects of Ramp Span and Deflection Angle on Laminar Boundary-Layer Separation at Mach 10.03," NASA TN D-2833 (1965).

11. Thareja, R. R., Prabhu, R. K., Morgan, K., Peraire, J., Peiro, J. and Soltani, S., "Applications of an Adaptive Unstructured Solution Algorithm to the Analysis of High Speed Flows," AIAA Paper 90-0395 (1990).